Carbon 208 (2023) 160–169

Contents lists available at ScienceDirect

Carbon

journal homepage: www.elsevier.com/locate/carbon

Intercalated oligomer doubles plasticity for strong and conductive graphene papers and composites

Kai Shen [a,1], Peng Li [a,1,**], Jiahao Lin [a], Ziqiu Wang [a], Gangfeng Cai [a], Xin Ming [a], Yingjun Liu [a], Chao Gao [a,b,*], Zhen Xu [a,b,***]

[a] MOE Key Laboratory of Macromolecular Synthesis and Functionalization, International Research Center for X Polymers, Department of Polymer Science and Engineering, Zhejiang University, 38 Zheda Road, Hangzhou, 310027, PR China
[b] Shanxi-zheda Institute of Advanced Materials and Chemical Engineering, Taiyuan, 030032, PR China

ARTICLE INFO

Keywords:
Oligomer intercalation induced plasticity
Graphene papers
Aligned fine wrinkles
Mechanical properties
High-performance composites
Electromagnetic interference shielding

ABSTRACT

Disordered wrinkles inevitably appear in the fluid assembly process of graphene and heavily depress performances of assembled graphene papers. Achieving high plasticity enables the post modulation to rearrange wrinkles by stretching. Here, we obtain an over 100% improved plasticity by intercalating oligomer into graphene oxide (GO) laminates and fabricate strong, stiff and conductive graphene papers (GPs) via post stretching. The intercalated oligomer activates the mobilization of GO sheets and achieves high plasticity of solid GO papers. The improved plasticity allows high stretching ratio and the post-stretched GP features regular orientation (0.95) of graphene sheets and aligned fine wrinkles. The crystalline GPs have a high tensile strength up to 1.3 GPa, Young's modulus of 92.9 GPa and highly electrical conductivity (1.05×10^5 S m^{-1}). The greatly improved plasticity by oligomer extends the processing capability of graphene materials and the strong and conductive GP can be assembled in high performance nanocomposites with excellent electromagnetic interference shielding effectiveness (EMI SE).

1. Introduction

Graphene has unprecedented in-plane mechanical and electrical properties, including fracture strength of 130 GPa, Young's modulus of 1 TPa and high electrical conductivity [1,2]. Macroscopic graphene materials have been designed by directly assembling single-layer graphene-derivatives (such as graphene oxide, GO) through a simple wet-assembly approach and a post chemical/thermal reduction. For example, graphene papers (GPs) can be prepared by solution casting [3–10], vacuum-assisted filtration [11–20], and spray coating [21,22]. Graphene fibers can be fabricated by wet-spinning of GO liquid crystals [23]. A vital goal is to realize the properties of single-layer graphene on the nanoscale into these macroscopic graphene materials, whereas limited by inevitably generated disorders in the wet-assembly process [24–26]. The low bending rigidity of GO sheets aggravates the formation of massive disorders during wet-assembly process [27,28], driven by the slow dynamic motion, skinning effect, and capillary contraction in drying [25]. How to eliminate these random disorders in macroscopic graphene materials has become a persistent challenge.

Several efforts have focused on reducing the random disorders in graphene papers. For instance, weakly oxidized graphene fabricated by a modified Hofmann's method has a higher bending rigidity and its paper exhibits enhanced sheet alignment of 0.84 with high tensile strength of 445 MPa and stiffness of 52.3 GPa [29]. By improving the pre-order of GO sheets in the liquid state, Zhong et al. reported a centrifugal spray method and prepared strong graphene papers with a high tensile strength of 660 MPa [22]. Very recently, a phenomenon of solvent intercalation plasticization was found to make GO papers (GOPs) with a near-solid plastic processing state, which allows the post-stretching to efficiently eliminate random wrinkles [30]. In the case of ethanol as intercalator, the ultimate strain was improved to 10% and the post-stretched GP exhibited a tensile strength of 1.1 GPa and a

* Corresponding author. MOE Key Laboratory of Macromolecular Synthesis and Functionalization, International Research Center for X Polymers, Department of Polymer Science and Engineering, Zhejiang University, 38 Zheda Road, Hangzhou, 310027, PR China.
** Corresponding author.
*** Corresponding author. Shanxi-zheda Institute of Advanced Materials and Chemical Engineering, Taiyuan, 030032, PR China.
E-mail addresses: pengli512@zju.edu.cn (P. Li), chaogao@zju.edu.cn (C. Gao), zhenxu@zju.edu.cn (Z. Xu).
[1] These authors contributed equally to this work.

https://doi.org/10.1016/j.carbon.2023.03.036
Received 20 January 2023; Received in revised form 15 March 2023; Accepted 16 March 2023
Available online 16 March 2023

Young's modulus of 62.8 GPa. In principle, the higher plastic deformation is achieved, the higher stretching-ratio can be applied to fully eliminate structural disorders and improve performances. How to promote the plastic deformation of solid GOPs and even exceed that of polymers still waits to be explored [30–33].

Here, we achieve an enlarged plasticity in GOP with plastic deformation exceeding 20% by intercalating oligomer into the interlayer of GO laminates. The ultimate strain of GOP by intercalating oligomer is twice as much as that by intercalating solvents at the same interlayer distance. We demonstrate that the improved plastic deformation mainly arises from the high inner friction of oligomer chains between adjacent GO sheets, which dramatically increases the energy-dissipation during stretching. The enhanced plasticity allows improved stretching ratio (SR) to adequately eliminate the disorders in the GP with a high sheet-orientation of 0.95. Massive aligned fine wrinkles in highly stretched GPs afford efficient stress-transfer under tension. The GP displays improved mechanical properties, including a high tensile strength of 1.3 GPa and Young's modulus of 92.9 GPa. Moreover, the electrical conductivity reaches 1.05×10^5 S m^{-1} after chemical reduction at room temperature. We also show a strong and functional composite with a layer-by-layer structure. The composite exhibits a high tensile strength and attractive electrical conductivity, extending the potential uses of graphene in EMI shielding.

2. Experimental section

2.1. Materials

Aqueous GO dispersion (11.7 mg g^{-1}) was purchased from Hangzhou Gaoxi Technology Co. Ltd (www.gaoxitech.com). The average size of GO was measured as 11.9 μm (Fig. S1). Polyethylene glycol (PEG, average molecular weight = 150, 200, 1000, 2000, 4000, 10000 Da) and ethanol were purchased from Macklin Biochemical Co. Ltd. Hydroiodic acid was purchased from Sinopharm Chemical Reagent Co., Ltd.

2.2. Preparation of GOP-i-PEG

PEG was mixed with diluted GO dispersions with a concentration of 6.5 mg g^{-1}. With a fixed GO mass of 0.1 g, we prepared six solutions with different GO and PEG concentrations: (1) 100 wt% GO and 0 wt% PEG; (2) 90 wt% GO and 10 wt% PEG; (3) 70 wt% GO and 30 wt% PEG; (4) 50 wt% GO and 50 wt% PEG; (5) 70 wt% GO and 30 wt% PEG; (6) 10 wt % GO and 90 wt% PEG. The GOP-i-PEG was prepared by casting the GO/PEG complex solutions on a polyethylene terephthalate (PET) substrate at ambient temperature and relatively high humidity for slow dehydration.

2.3. Plastic stretching of GOP-i-PEG

The plastic GOP-i-PEG was stretched at different SR (0%, 8%, 15%) with a speed of 5 mm min^{-1}. Then, in the tension state, stretched GOP-i-PEG was immersed in ethanol for at least 10 min to remove the PEG. Finally, the plastic-stretched GOP was obtained after drying under tension at ambient temperature.

2.4. Preparation of GP

Followed by reduction with the mixture of hydroiodic acid and ethanol (the volume ratio of 1:3) at room temperature for 24 h, GP was obtained after being washed repeatedly with ethanol five times, and completely dried under tension at ambient temperature.

2.5. Fabrication of GP/epoxy resin laminated composites

GPs and epoxy resin were alternatively put on a flat Teflon plate. Then, a fixed pressure of 10 MPa was applied and the temperature was kept at 80 °C. After 12 h, the GP/epoxy resin laminated composite was obtained.

2.6. Characterization

Mechanical tests were taken on Instron 2344 at a loading rate of 5 mm min^{-1}. The size of tested samples was 15 mm × 1 mm and the gauge length was 10 mm. The dynamic mechanical analysis was performed on a DMA 242E (NETZSCH Instruments) at a varied frequency at room temperature. For stress relaxation experiments, samples were stretched to the same strain, followed by maintaining the strain while the evolution of stress with time was recorded. Scanning electron microscope (SEM) images were taken on a Hitachi S4800 field-emission SEM system. Polarized optical microscopy (POM) characterizations were performed using Nikon, E600POL. 3D-Profile images were taken using an optical profilometer (Wyko NT9100). XRD profiles were collected on a X'Pert Pro (PAN analytical) diffractometer using monochromatic Cu 17 Kα1 radiation ($\lambda = 1.5406$ Å) at 40 kV. Electrical conductivity was measured using a four-probe method on a Keithley 2400 multiple-function source-meter. Thermal Gravimetric Analyzer (TGA) tests were carried out using a thermogravimetric analyzer (PerkinElmer Pyris 1). UV–vis absorption spectra of GOPs were collected using an ultraviolet spectrophotometer (UV 2450, Shimadzu, Japan). Wide-angle X-ray scattering (WAXS) measurements were carried out on the BL16B1 beamline station in Shanghai Synchrotron Facility (SSRF). Samples were prepared by aligning papers on the side of quartz plate for the transmission test mode. Raman measurements were performed on a Renishaw in Via-Reflex at an excitation wavelength of 532 nm. High resolution transmission electron microscope (HR-TEM) images were taken on a JEM-2100F field-emission TEM system. The Fourier transform infrared spectroscopy (FT-IR) was taken by Nicolet iS20. X-ray photoelectron spectroscopy (XPS) characterization was operated at 14.0 kV with a PHI 5000 C ESCA system and all binding energies are referenced to C_{1s} neutral carbon peak at 284.8 eV. The electromagnetic interference shielding effectiveness (EMI SE) was tested by a vector network analyzer (ZNB-40, Rohde & Schwarz, Germany). EMI SE was calculated with those scattering parameters (S_{11}, S_{22}, S_{12}, S_{21}) obtained by vector network analyzer:

$$R = S_{11}^2 = S_{22}^2 \tag{1}$$

$$T = S_{12}^2 = S_{21}^2 \tag{2}$$

$$A = 1 - R - T \tag{3}$$

$$SE_T = -10\, log_{10}\, T \tag{4}$$

$$SE_R = -10\, log_{10}(1 - R) \tag{5}$$

$$SE_A = SE_T - SE_R \tag{6}$$

where R, T and A represent the reflection, transmission and absorption power coefficients, respectively. SE_T, SE_R, and SE_A represent the total, reflective, and absorptive SE, respectively.

3. Results and discussion

3.1. Oligomer enhanced plasticity

Generally, GOPs are brittle because of the strong interlayer interaction (Fig. 1a). They show a typically elastic deformation with an elongation at break of only 3.8%, which indicates the brittle fracture feature (Fig. 1a, Model I). This intrinsic elastic deformation and fracture behavior of GO make it impossible to eliminate the random disorders in GOPs. A new state of plasticity was invented by intercalating ethanol into GOPs [30]. As the interlayer spacing increases, the van der Waals interaction between adjacent GO layers is severely reduced (denoted as

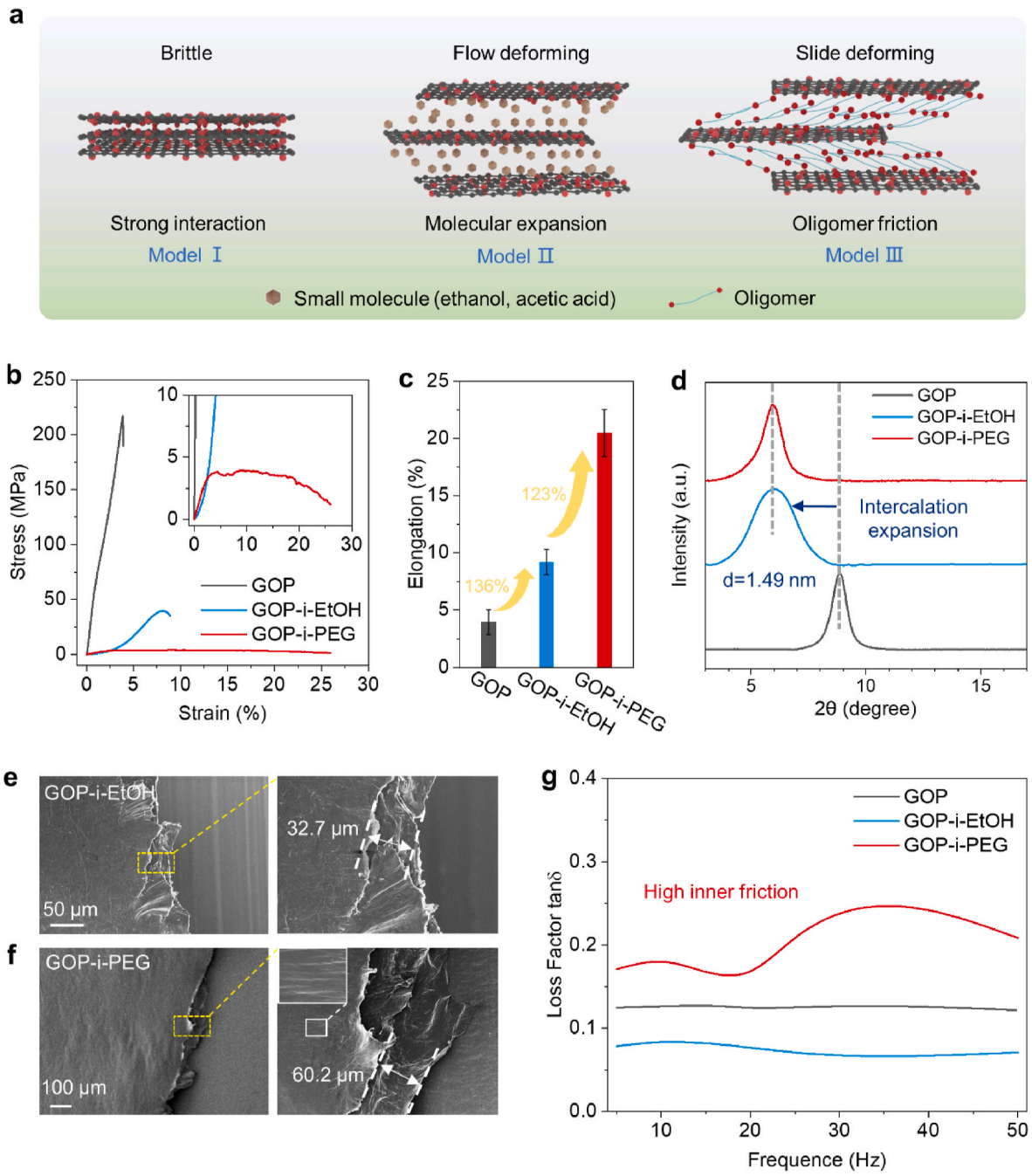

Fig. 1. Plasticization of GO laminates. (a) Schematic of the three tensile behavior of GO laminates. (b–d) Tensile curves (b), plasticity comparison (c), XRD patterns (d) of the plasticized GOP-i-PEG, GOP-i-EtOH and pristine GOP, respectively. The inset of (b) is the magnified tensile curve of GOP-i-PEG. (e, f) Fracture morphology of GOP-i-EtOH (e) and GOP-i-PEG (f), respectively. (g) DMA profiles of GOP, GOP-i-PEG and GOP-i-EtOH, respectively. (A colour version of this figure can be viewed online.)

GOP-i-EtOH). In this situation, the near-solid laminate (Fig. 1a, Model II) allows the GO sheets to move freely, giving the GOP an ultimate elongation of less than 10%.

We indicate that intercalating an oligomer, such as PEG, into the interlayer of GOPs will improve plastic deformation (denoted as GOP-i-PEG). The ultimate strain exceeds 20%, which is almost five times higher than that of pristine GOP, yet the tensile strength inversely decreases from 217 MPa to 4 MPa (Fig. 1b). When the interlayer distance of these two GOPs is approximately the same (around 1.49 nm) according to the XRD spectra in Fig. 1d, the ultimate elongation of GOP-i-PEG is 123% higher than that of GOP-i-EtOH (Fig. 1c). This indicates a hidden new mechanism for the plasticity of GOP aside from the increased interlayer spacing.

To uncover the mechanism of enhanced plasticity, fracture morphologies of pristine GOP, GOP-i-EtOH, and GOP-i-PEG were carefully compared. As shown in Fig. 1e and f, the plasticized GOP exhibits clear slide feature [34]. The slide distance of GOP-i-PEG is around 60.2 μm, almost twice as much as that (32.7 μm) of GOP-i-EtOH. In contrast, pristine GOP has negligible sheet-sliding of GO sheets (Fig. 1a, Model I and Fig. S3). Notably, the surface of GOP-i-PEG shows aligned texture and the crack tip becomes thinner, indicating the efficiently activated sheet-sliding and improved plasticity (Fig. S4). We attribute the improved plasticity to the higher inner friction of PEG chains between adjacent GO layers. Compared with GOP-i-EtOH and pristine GOP, the

GOP-i-PEG has a greater loss factor (Fig. 1g), indicating that there is more internal friction between the GO layers (Fig. 1a, Model III). These results demonstrate the enhanced inner friction in GOP-i-PEG, which dissipates large amount of energy and affords an efficient sliding deformation during stretching (Fig. 1a, Model III).

3.2. Critical interlayer distance and strong inner friction

To further optimize the plasticity and illustrate the plasticization mechanism, we investigated the plasticity of GOP-i-PEG with different PEG content. Fig. 2a shows typical tensile curves of GOP-i-PEG. With the intercalation of PEG, GOP displays a transition from the brittle state to the plastic state, showing reduced tensile strength and increased ultimate strain. The ultimate strain reaches a highest value of around 20% when PEG content is 70 wt%, yet begins to decrease at higher content. A critical interlayer distance d_c and optimized inner friction mutually determine the plasticity as shown in Fig. 2b and c. The interlayer distance d calculated by (001) peak of GOP-i-PEG in XRD is linear with the content of PEG (Fig. 2d and e) [32]. According to Lifshiz's formula [35], the van der Waals interaction between adjacent GO sheets is strongly determined by the interlayer distance as follows:

$$W_{vdW}(d) = -\frac{H}{12\pi}\left(\frac{1}{d^2}+\frac{1}{(d+2t)^2}-\frac{2}{(d+t)^2}\right) \quad (7)$$

where, H is Hamaker constant (determined by intercalator), d is the interlayer distance, and t is the thickness of GO sheets. When PEG content is lower than 70 wt%, the interlayer distance d is smaller than d_c, endowing GO sheets with poor movability. GOP-i-PEG at a high PEG content up to 90 wt% has a larger interlayer distance. Although the GO sheets could move freely, excess PEG inversely lubricate the adjacent GO sheets, yielding a weak inner friction and a decreased plastic deformation. A critical interlayer distance d_c of 1.49 nm occurs when PEG

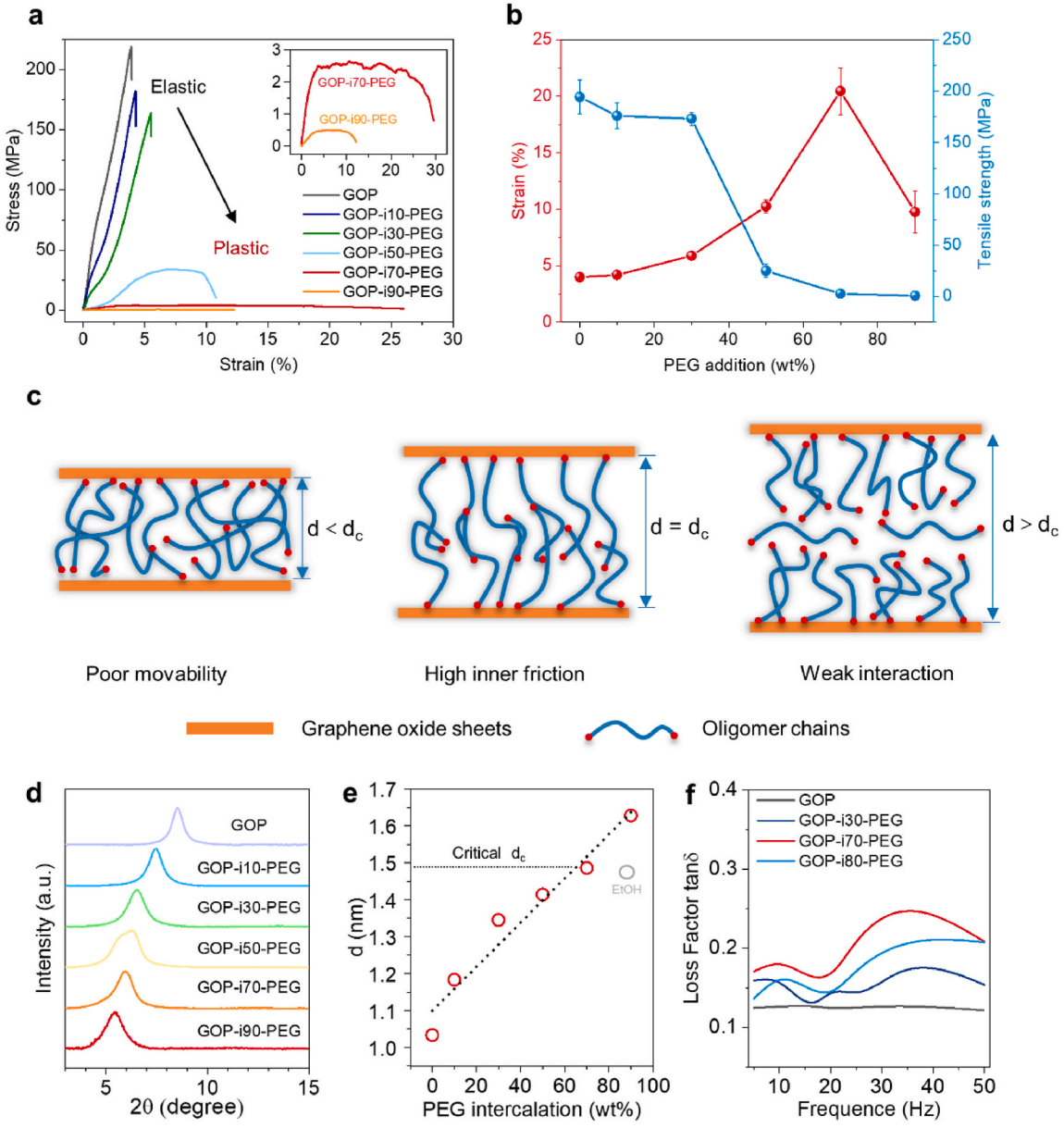

Fig. 2. Plasticization mechanism of oligomer intercalation. (a, b) Typical tensile curves (a) and statistical tensile strength and strain (b) of GOP-i-PEG with varied content of PEG (To clarify, GOP-i*n*-PEG means GOP with *n* wt% PEG). The inset tensile curves of (a) corresponds to GOP-i70-PEG and GOP-i90-PEG, respectively. (c) Schematic diagram illustrating the plasticization mechanism determined by interlayer distance and inner friction of PEG chains between GO sheets. (d–f) XRD patterns (d), interlayer distance (e) and loss factor (f) of GOP-i-PEG with varied content of PEG. (A colour version of this figure can be viewed online.)

content is 70 wt%. In this condition, GOP-i-PEG also has the largest loss factor (Fig. 2f), indicating the strong inner friction. Overall, expanded interlayer distance enables GO sheets to move, at the meantime, a strong inner friction dissipates massive energy during stretching, which jointly contribute to the improved plasticity.

In addition, GOPs intercalated with PEG of different molecular weight (*Mw*) were tested (Fig. S5). PEG with lower *Mw*, such as 150, 200, and 600, enables GOPs to show higher plastic deformation. PEG with higher *Mw* has a poor chain moveability, which immobilizes the sheet-sliding of GO at room temperature, and thus yields limited plasticity [32].

The enhanced plasticity affords the efficient post-processing of GOPs. For instance, the nanoimprinted sample shows accurate size control of the uniform and aligned solid columns with average diameter reaching 260 nm due to the increased plasticity (Fig. S6). In this study, we emphasize that the mobilized GO sheets with doubled plastic deformation can effectively eliminate the disorders in GPs by stretching.

3.3. Plasticization-stretching process

An improved plasticization-stretching process to reduce the random disorders in GOPs includes three vital steps (Fig. 3a): (1) Directly casting papers (GOP-i-PEG composed of 30 wt% GO and 70 wt% PEG, GOP-i70-PEG). (2) Stretching the GOP-i-PEG to a specific ratio. Given the improved plasticity, the GOP can be stretched with a SR from 0% to 15%. The stress is rapidly relaxed in the stretching process, thus maintaining the extended GO sheets in the stretched GOP (Fig. S7). (3) Removing PEG by immersing stretched GOP-i-PEG in ethanol for at least 10 min and drying under a tension to immobilize the extended GO sheets (Fig. S8). The thickness of GOP clearly decreases as the SR increases (Fig. S9 and Fig. S10). After chemical reduction, GPs exhibited bright silver and aligned surface texture (Fig. 3b), labeled as SR-GPs. The post plasticization-stretching method completes the structural control of GPs starting from the liquid state to the solid state, and thus produces high-quality GPs. To investigate the structural evolution and property enhancement, 8%-GP (the highest SR in previous report) was also fabricated to be a control sample.

3.4. Stretching induced high crystallinity and aligned fine wrinkles

Through the enhanced plasticization-stretching, the random disorders are largely reduced, affording a highly crystalline GP. From XRD spectra, the full-width at half-maximum (FWHM) of the (002) crystalline plane gradually decreased from 1.98° for pristine GP to 0.98° for 15%-GP and the corresponding crystalline thickness was calculated from 4.4 nm to 8.8 nm (Fig. 3c and d), indicating the improved crystallinity [36]. We

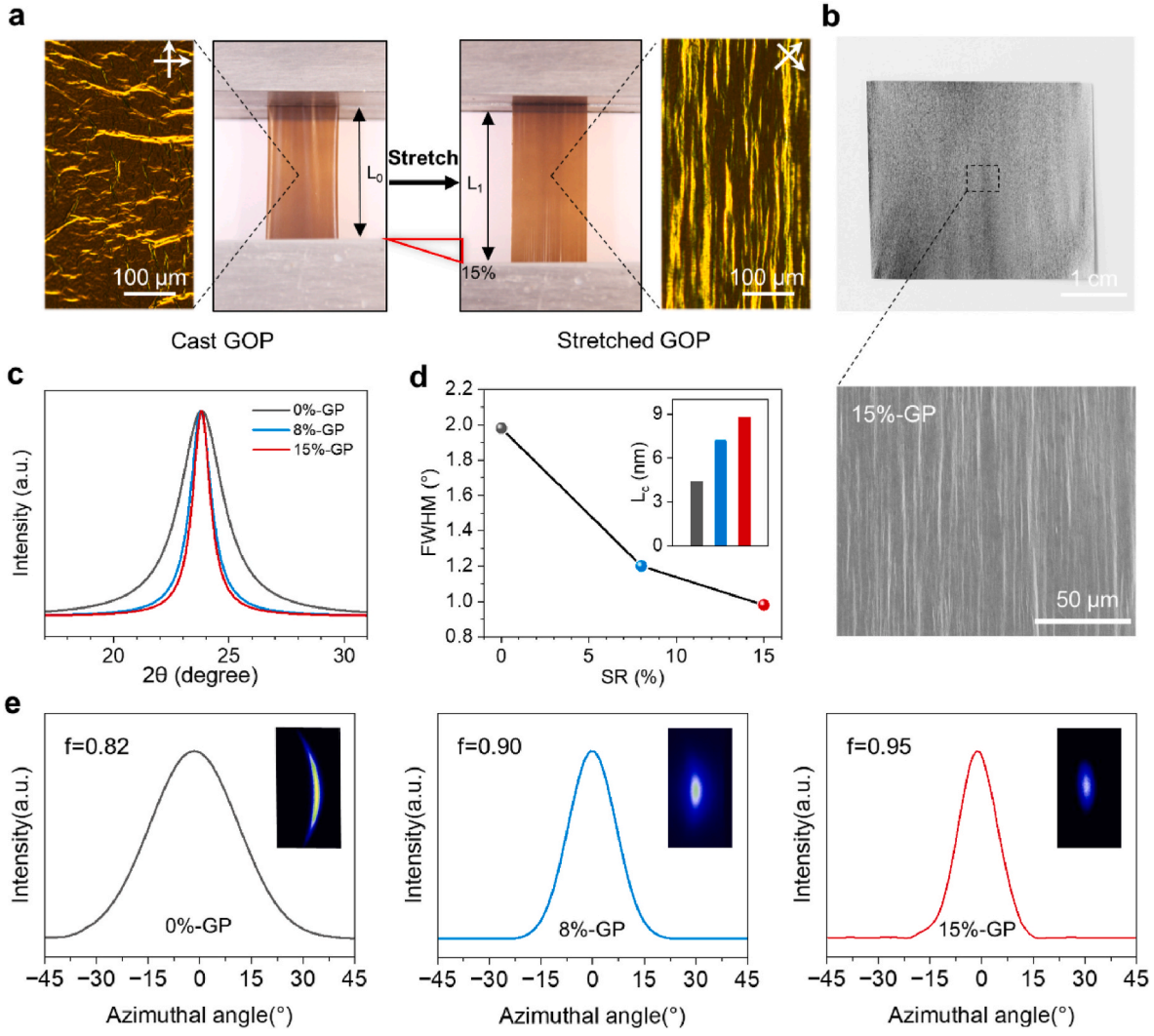

Fig. 3. Structural analysis of GPs at different SR. (a) Process of plasticization stretching. (b) Photograph and SEM image of 15%-GP. (c) XRD profiles of GPs at different SR. (d) FWHM of (002) peak in (c) together with corresponding crystalline thickness (L_c, inset). (e) WAXS patterns and the corresponding azimuthal scan curves of GPs at different SR. (A colour version of this figure can be viewed online.)

further evaluated the orientation order of graphene sheets calculated from azimuthal integrated curves in WAXS tests (Fig. 3e) [37,38]. The orientation order parameter of 15%-GPs is 0.95, 16% higher than that of pristine GP, reaching the reported highest value of neat GP [17,18,20,29,30,37,38]. XPS and FT-IR results reveal that after chemical reduction, substantial oxygen-containing functional groups, such as the hydroxyl group, had been eliminated, and the sp^2 structure had been highly restored (Fig. S12 and Fig. S13). TEM images intuitively show the aligned graphene sheets in 15%-GP, distinct from the random arrangement in pristine GP (Fig. S14) [39].

The wrinkle morphology on the surface also reflects the crystalline order of graphene sheets [26,40]. We revealed that the random wrinkle network on the pristine GP is stretched to be aligned along the stretching direction in both 8%-GP and 15%-GP (Fig. 3b and Fig. S18). The wavelength (λ_w) of aligned wrinkles is gradually reduced with higher SR (Fig. 4a). The surface height profile image (at a high magnification of × 100) shows distributed aligned fine wrinkles on the 15%-GP, whereas it exhibits thick and relatively random wrinkles on the 8%-GP (Fig. 4b and Fig. S19). The corresponding average power spectrum density (PSD) from height profiles of wrinkles was calculated (Fig. 4c and Fig. S20). A peak positioned at higher frequency occurs in 15%-GP, which means a smaller λ_w of adjacent fine wrinkles [24,40]. The average λ_w of wrinkles of 15%-GP is less than 9.9 μm, 35% and 67% narrower than that of 8%-GP (15.3 μm) and 0%-GP (29.8 μm), respectively (Fig. 4d). We further concluded the fractal wrinkle structure by analyzing the surface height profile images at varied magnifications (Fig. 4e and Figs. S21–22). The wrinkle λ_w of 15%-GP at any magnification is smaller than that of pristine GP and 8%-GP. The orientation is also calculated from the azimuthal angular integral of 2D FFT images (Fig. 4f and Fig. S23) [41], which can be equivalent to be the orientation order of wrinkles with specific λ_w. As shown in Figs. 4g and 15%-GP shows the same high orientation order of fine wrinkles with the λ_w ranging from 9.9 μm to 127.2 μm. As a comparison, 8%-GP has large wrinkles of 169.4 μm with an orientation order of 0.90. But the orientation decreases to 0.69 for minor wrinkles, indicating that insufficient plasticization SR cannot fully eliminate the random disorders. Overall, the highly improved plasticity enables the accurate control of the GP microstructure and achieve higher crystalline order.

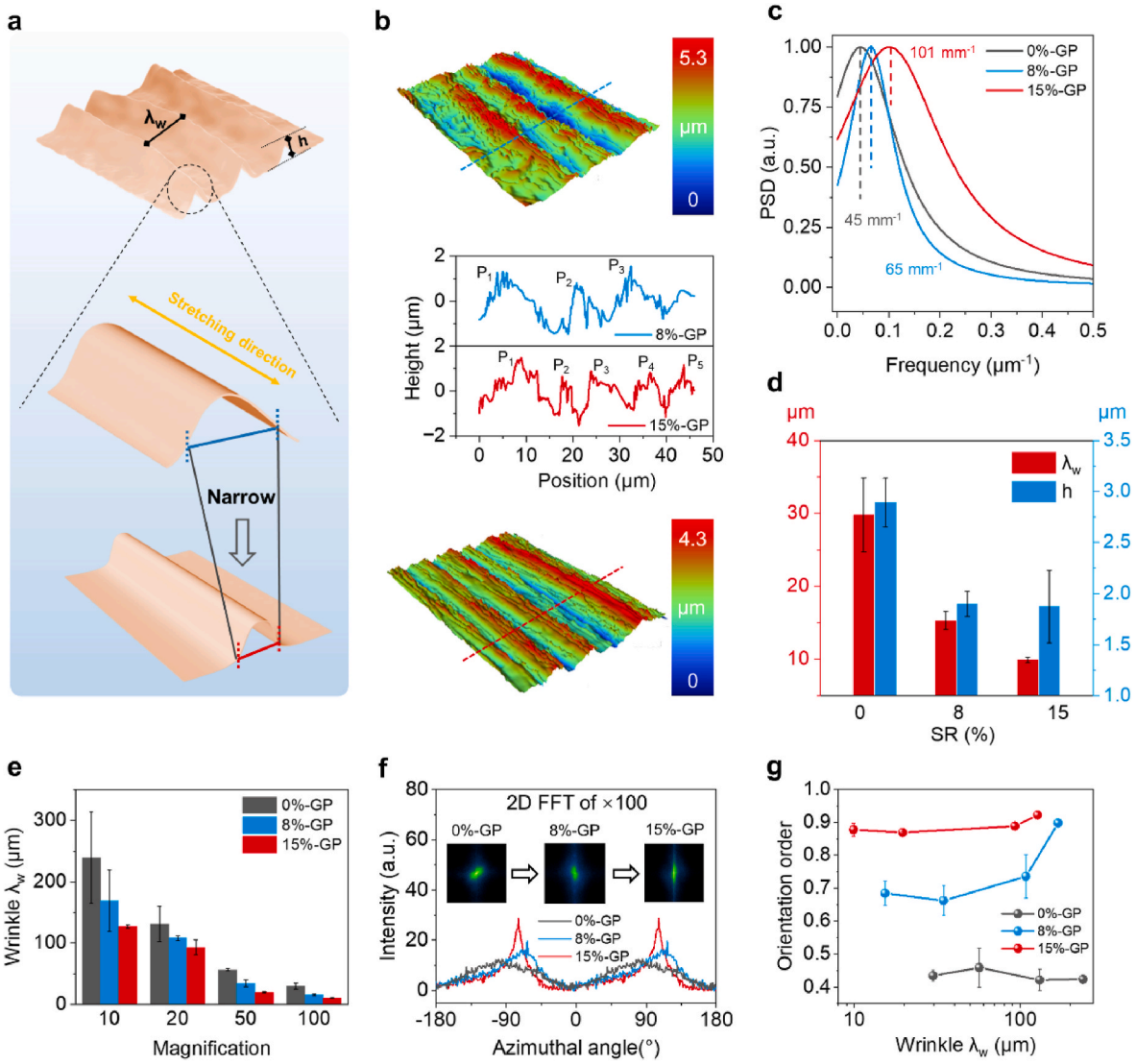

Fig. 4. Wrinkle analysis of GPs at different SR. (a) Schematic depicting the variation of wrinkles of GOPs after stretching. (b) Profile images of 8%-GP (top) and 15%-GP (bottom) and their typical height profiles (middle) at a high magnification of 100 (× 100). (c) PSD spectra with a function of frequency of GPs at different SR (× 100), averagely calculated from 1D FFT of the height profiles in (b). (d) The statistical wavelength λ_w and height (h) of wrinkles in GPs (× 100). (e) The wrinkle wavelength λ_w of GPs at varied magnifications, showing finer wrinkles generated in 15%-GPs at any magnification. (f) 2D FFT images and the corresponding azimuthal scan curves of GPs at different SR (× 100). (g) Orientation order of wrinkles in GPs at different SR. (A colour version of this figure can be viewed online.)

3.5. Mechanical and electrical properties of the GPs

The increased plasticization stretching provides GPs with highly aligned fine wrinkles and enhanced crystalline order, which improves mechanical properties. As shown in Fig. 5a and b, with the increasing SR, the tensile strength and Young's modulus are synergistically increased. The modulus of 15%-GPs reaches 92.9 GPa, 868% and 88% higher than those of pristine GPs (9.6 GPa) and 8%-GPs (49.4 GPa), respectively. Compared with previous crystalline GP via stretching the plasticized GOP by intercalating ethanol [30], the oligomer intercalated GOP shows enlarged plastic deformation and has a higher SR of 15%, thus improving the stiffness by 48%. We revealed that the high Young's modulus comes from the improved orientation of graphene sheets. As shown in Fig. 5c, the modulus has a positive correlation with the orientation order of graphene sheets calculated from WAXS patterns.

The tensile strength of 15%-GP was measured as 1.3 GPa, 397% and 69% higher than that of pristine GPs (261.5 MPa) and 8%-GPs (769.2 MPa), respectively. The high tensile strength mainly results from the highly aligned fine wrinkles, which average the load under tension and enhance the load transfer. We demonstrated that 15%-GP with highly aligned fine wrinkles (λ_w = 9.9 μm) has a higher efficiency of load transfer. Rapid downshift of G-band to lower frequency indicates the higher load transfer when tensile strain is applied [42–44]. As shown in Fig. 5d and Fig. S24, 15%-GP has a remarkable downshift of G peak reaching 14.5 cm^{-1} per 1% strain, much higher than that of pristine GP (1.4 cm^{-1} per 1% strain) and 8%-GP (8.7 cm^{-1} per 1% strain) as the applied strain increases.

The high stiffness and superior tensile strength enable the GP to be a potential candidate of structural materials (Fig. 5e) [45,46]. The highly extended graphene sheets immobilized during drying also endows 15%-GP with a dramatical advantage in resistance to stress relaxation (Fig. S25). Furthermore, because of the highly crystalline order, the 15%-GP displays a dramatically enhanced electrical conductivity by about 891% compared with the pristine GP (Fig. 5f). 15%-GPs also show excellent EMI SE (24.4 dB in 2–18 GHz), with SE_A accounting for roughly 70% of SE_T (Fig. S26). The contribution of relaxation loss to SE_T is negligible, because abundant polar oxygen-containing groups are removed after chemical reduction (Fig. S12 and Fig. S13) [47,48]. Therefore, conduction loss driven by high electrical conductivity mainly contributes to the high EMI SE [49].

3.6. High-performance GP-based composites

Using GP as a component, we further fabricated a laminated composite of epoxy resin with an alternatively layered structure by the thermal-compression technique [50,51]. As shown in Fig. 6c, GP spreads out the whole composite and few destructive interfaces, such as voids, are observed. Therefore, the merit of high performance of crystalline GPs has been achieved in the prepared GP/epoxy resin composite. For example, the composite shows a high tensile strength of 766.7 MPa and a modulus of 52.2 GPa, 534% and 965% higher than those of pure epoxy resin, respectively (Fig. 6d). Given the highly electrical conductivity of the crystalline GP, the composite also displays a superior electrical conductivity of 6.6 × 10^4 S m^{-1} (Fig. 6d). We demonstrate that the GP-based composite exhibits an outstanding EMI shielding performance with average effectiveness of 43.9 dB in 2–18 GHz, which is much higher than that (5 dB) of pure epoxy resin (Fig. 6e). Benefiting from the layered structure of the conductive composite, electromagnetic waves are reflected repeatedly after their interaction with the carriers on the surface of graphene. The remaining electromagnetic waves pass through the interior of the conductive composite and are largely absorbed by multiple reflection and scattering inside the layered structure. In addition, the decreased electrical conductivity of GP/epoxy composite compared with pure GP weakens impedance mismatching between the electromagnetic wave and the composite, thus resulting in lower SE_R. As a result, SE_A made up nearly 93% of SE_T, much higher than that (70%) of GP with single layer (Fig. 6f and Fig. S26).

We systematically investigated the effect of the number of stacked layers, the pressure and temperature on the EMI shielding performance (Fig. S31). A positive relationship between the EMI shielding

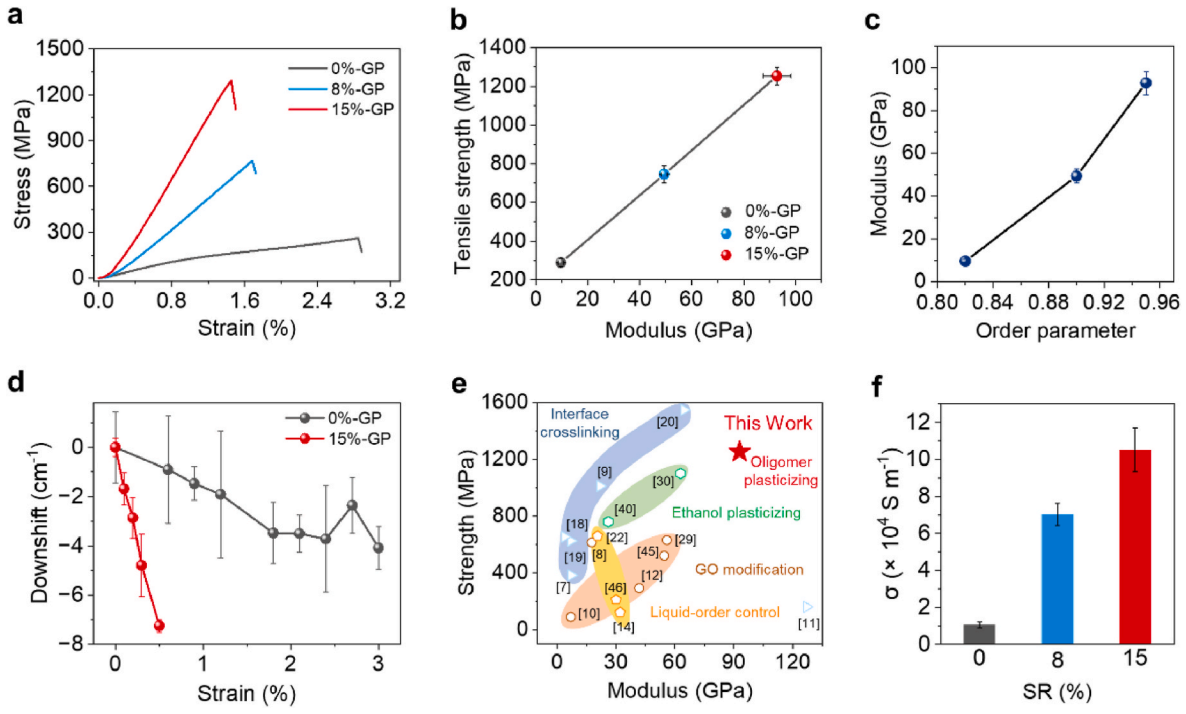

Fig. 5. Mechanical and electrical properties of GPs. (a) Typical tensile curves of GPs at different SR. (b) Tensile strength and Young's modulus of GPs at different SR. (c) Relationship between Young's modulus and orientation order of graphene sheets calculated from WAXS patterns. (d) The downshift of Raman G-band frequency versus applied strain for 0%-GP and 15%-GP, respectively. (e) Comparison of strength and modulus of 15%-GP with previous reported GPs. (f) Electrical conductivity of GPs at different SR. (A colour version of this figure can be viewed online.)

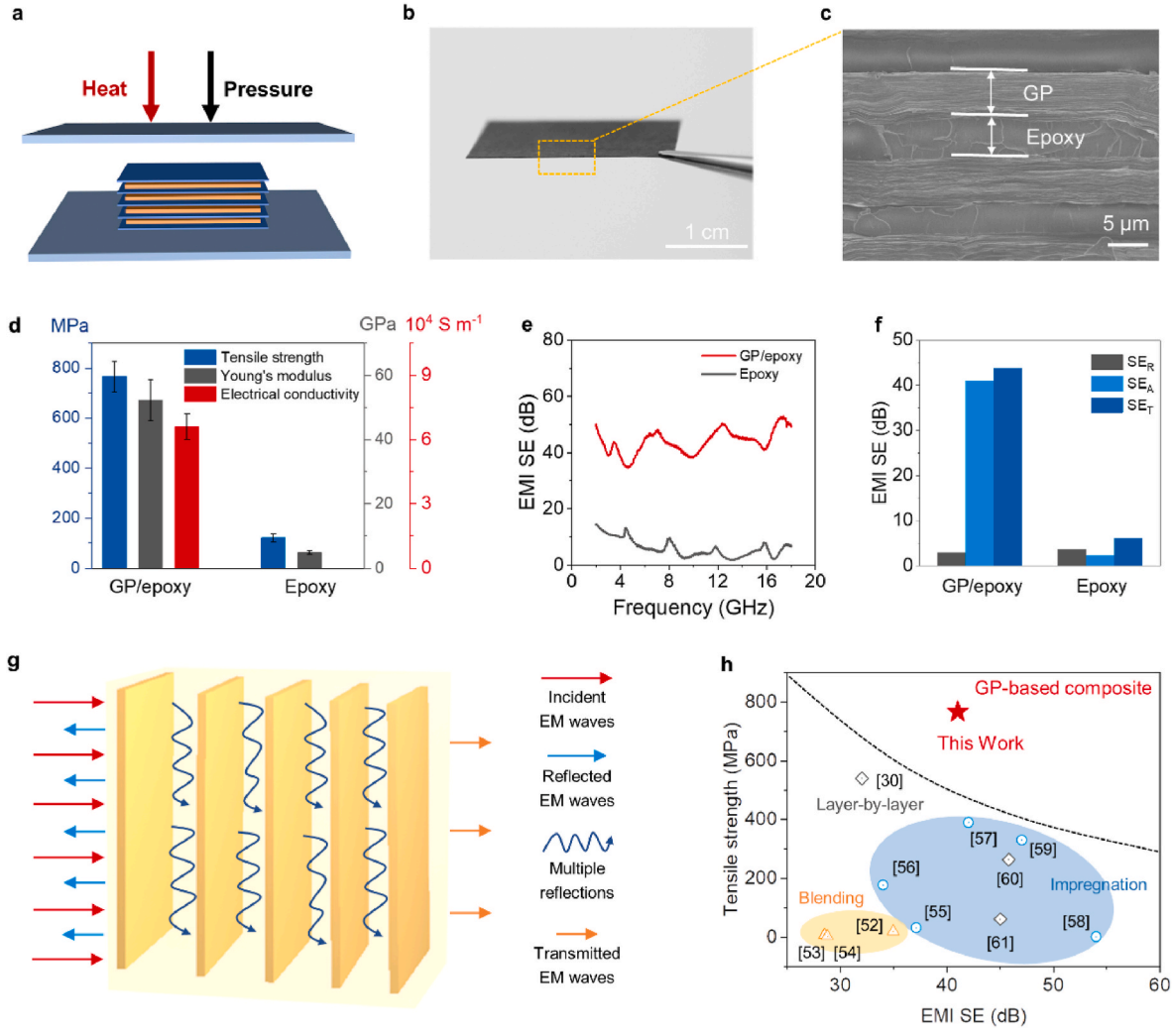

Fig. 6. GP/epoxy resin laminated composites. (a) Schematic of the fabrication of the layer-by-layer structured GP/epoxy resin composites. (b, c) Photograph (b) and SEM images (c) of the laminated composites. (d, e) Comparison of tensile strength, Young's modulus and electrical conductivity (d) and EMI SE (e) between the 15%-GP/epoxy and epoxy resin. (f) SE_T, SE_A and SE_R in 2–18 GHz of 15%-GP/epoxy and epoxy resin. (g) Schematic of the EMI shielding mechanism of the layer-by-layer structured composite. (h) Comparison of tensile strength and EMI SE of the 15%-GP/epoxy with previous reported graphene-based composite for EMI shielding. (A colour version of this figure can be viewed online.)

performance and the number of stacking layers is revealed. But the pressure and temperature in the hot-pressing process have little influence on the EMI SE, yet affect the solidifying time and structural porosity (Fig. S31 and Fig. S32).

The integration of superior mechanical strength, low density (1.50 g cm^{-3}), electrical conductivity and high EMI SE of the GP-based composite makes it a potential structural and functional material in electromagnetic devices. Previous reports on preparing graphene-based electromagnetic shielding composites mainly adopt two strategies including directly blending graphene sheets to matrix and infiltrating polymer into a graphene framework [52–61]. Although the direct blending is the most convenient method, it has a disadvantage of poor connection of graphene sheets. The resulting composites show inferior EMI shielding performance and mechanical properties. Infiltrating polymer into a well-connected graphene network (even annealed over 1000 °C) improves the electrical conductivity and EMI shielding performance. However, the fragile graphene aerogel fails the expectation of simultaneously strengthening the composites. Our layer-by-layer structured composite by using strong, stiff and conductive GPs as assembly units successfully integrates high tensile strength and superior EMI shielding performance (Fig. 6h). These GP-based nanocomposites will greatly broaden the realistic uses of graphene and its macroscopic materials.

4. Conclusion

In summary, we achieved an over 100% improvement of plasticity of GOP by intercalating oligomer than that of GOP intercalated with ethanol, which originates from the combination of activated sheet-mobility at a critical interlayer distance and strong inner friction between GO layers. Such a good plasticity guarantees to fully eliminate the random disorders and improve the orientation order of GPs by efficient stretching. Massive aligned fine wrinkles generated during the stretching process, largely promoting the stress transfer under tension. Therefore, GPs composed of neat graphene sheets show a record-high tensile strength, Young's modulus and superior electrical conductivity. GP-based nanocomposites with the layer-by-layer structure also achieve high EMI SE originating from the excellent properties of the GPs, extending the realistic uses of graphene in structural materials, engineering and EMI shielding. This work could not only enhance the understanding of the plasticity nature in GO assemblies but also guide the preparation of high-performance GPs for future industrial application.

CRediT authorship contribution statement

Kai Shen: Investigation, Methodology, Formal analysis, Writing – original draft. **Peng Li:** Formal analysis, Visualization, Writing – review & editing, Supervision. **Jiahao Lin:** Formal analysis, Visualization. **Ziqiu Wang:** Investigation, Validation. **Gangfeng Cai:** Methodology. **Xin Ming:** Investigation. **Yingjun Liu:** Formal analysis. **Chao Gao:** Conceptualization, Supervision, Funding acquisition. **Zhen Xu:** Conceptualization, Writing – review & editing, Project administration.

Declaration of competing interest

The authors declare that they have no known competing financial interests or personal relationships that could have appeared to influence the work reported in this paper.

Acknowledgements

We thank the staff at the Shanghai Synchrotron Radiation Facility (SSRF) for assistance in WAXS characterizations, and we acknowledge the technical support by Liying Chen, State Key Laboratory of Modern Optical Instruments, Zhejiang University. This work is supported by the National Natural Science Foundation of China (Nos. 52090030, 51973191, 52122301 and 51533008), the Fundamental Research Funds for the Central Universities (No. K20200060, 2017QNA4036, 2017XZZX001-04), Hundred Talents Program of Zhejiang University (188020*194231701/113), Postdoctoral Research Program of Zhejiang Province (ZJ2022079), Shanxi-zheda Institute of New Materials and Chemical Engineering (Nos. 2022SZ-TD012, 2022SZ-TD011 and 2021SZ-FR004) and the International Research Center for X Polymers.

Appendix A. Supplementary data

Supplementary data to this article can be found online at https://doi.org/10.1016/j.carbon.2023.03.036.

References

[1] A.K. Geim, Graphene: status and prospects, Science 306 (2009) 666–669.
[2] A.K. G, K.S. Novoselov, S.V. Morozov, S.V. Dubonos, I.V. Grigorieva, A.A. Firsov, Electric field effect in atomically thin carbon films, Science 324 (2004) 1530–1534.
[3] L. Huang, C. Li, W. Yuan, G. Shi, Strong composite films with layered structures prepared by casting silk fibroin-graphene oxide hydrogels, Nanoscale 5 (9) (2013) 3780–3786.
[4] L. Peng, Z. Xu, Z. Liu, Y. Guo, P. Li, C. Gao, Ultrahigh thermal conductive yet superflexible graphene films, Adv. Mater. 29 (27) (2017), 1700589.
[5] Y. Wen, M. Wu, M. Zhang, C. Li, G. Shi, Topological design of ultrastrong and highly conductive graphene films, Adv. Mater. 29 (41) (2017), 1702831.
[6] Y. Xiao, Z. Xu, Y. Liu, L. Peng, J. Xi, B. Fang, F. Guo, P. Li, C. Gao, Sheet collapsing approach for rubber-like graphene papers, ACS Nano 11 (8) (2017) 8092–8102.
[7] M. Zhang, L. Huang, J. Chen, C. Li, G. Shi, Ultratough, ultrastrong, and highly conductive graphene films with arbitrary sizes, Adv. Mater. 26 (45) (2014) 7588–7592.
[8] M. Zhang, Y. Wang, L. Huang, Z. Xu, C. Li, G. Shi, Multifunctional pristine chemically modified graphene films as strong as stainless steel, Adv. Mater. 27 (42) (2015) 6708–6713.
[9] S. Jin, B. Chung, H.J. Park, B.V. Cunning, J.H. Lee, A. Yoon, M. Huang, H. Seo, D. Lee, Z. Lee, R.S. Ruoff, S. Ryu, Ultrahigh strength and modulus graphene-based hybrid carbons with AB-stacked and turbostratic structures, Adv. Funct. Mater. 30 (50) (2020), 2005381.
[10] S. Wang, X. Sun, F. Xu, M. Yang, W. Yin, J. Li, Y. Li, Strong yet tough graphene/graphene oxide hybrid films, Carbon 179 (2021) 469–476.
[11] Z. An, O.C. Compton, K.W. Putz, L.C. Brinson, S.T. Nguyen, Bio-inspired borate cross-linking in ultra-stiff graphene oxide thin films, Adv. Mater. 23 (33) (2011) 3842–3846.
[12] H. Chen, M.B. Müller, K.J. Gilmore, G.G. Wallace, D. Li, Mechanically strong, electrically conductive, and biocompatible graphene paper, Adv. Mater. 20 (18) (2008) 3557–3561.
[13] Q. Cheng, M. Wu, M. Li, L. Jiang, Z. Tang, Ultratough artificial nacre based on conjugated cross-linked graphene oxide, Angew. Chem. Int. Ed. 152 (13) (2013) 3838–3843.
[14] D.A. Dikin, S. Stankovich, E.J. Zimney, R.D. Piner, G.H. Dommett, G. Evmenenko, S.T. Nguyen, R.S. Ruoff, Preparation and characterization of graphene oxide paper, Nature 448 (7152) (2007) 457–460.
[15] L. Dong, Z. Chen, S. Lin, K. Wang, C. Ma, H. Lu, Reactivity-controlled preparation of ultralarge graphene oxide by chemical expansion of graphite, Chem. Mater. 29 (2) (2017) 564–572.
[16] Y. Tian, Y. Cao, Y. Wang, W. Yang, J. Feng, Realizing ultrahigh modulus and high strength of macroscopic graphene oxide papers through crosslinking of mussel-inspired polymers, Adv. Mater. 25 (21) (2013) 2980–2983.
[17] S. Wan, Y. Li, J. Mu, A.E. Aliev, S. Fang, N.A. Kotov, L. Jiang, Q. Cheng, R. H. Baughman, Sequentially bridged graphene sheets with high strength, toughness, and electrical conductivity, Proc. Natl. Acad. Sci. USA 115 (21) (2018) 5359–5364.
[18] T. Zhou, H. Ni, Y. Wang, C. Wu, H. Zhang, J. Zhang, A.P. Tomsia, L. Jiang, Q. Cheng, Ultratough graphene-black phosphorus films, Proc. Natl. Acad. Sci. USA 117 (16) (2020) 8727–8735.
[19] Y. Wang, F. Meng, F. Huang, Y. Li, X. Tian, Y. Mei, Z. Zhou, Ultrastrong carbon nanotubes/graphene papers via multiple pi-pi cross-linking, ACS Appl. Mater. Interfaces 12 (42) (2020) 47811–47819.
[20] S. Wan, Y. Chen, S. Fang, S. Wang, Z. Xu, L. Jiang, R.H. Baughman, Q. Cheng, High-strength scalable graphene sheets by freezing stretch-induced alignment, Nat. Mater. 20 (5) (2021) 624–631.
[21] G. Xin, H. Sun, T. Hu, H.R. Fard, X. Sun, N. Koratkar, T. Borca-Tasciuc, J. Lian, Large-area freestanding graphene paper for superior thermal management, Adv. Mater. 26 (26) (2014) 4521–4526.
[22] J. Zhong, W. Sun, Q. Wei, X. Qian, H.M. Cheng, W. Ren, Efficient and scalable synthesis of highly aligned and compact two-dimensional nanosheet films with record performances, Nat. Commun. 9 (1) (2018) 3484.
[23] Z. Xu, C. Gao, Graphene chiral liquid crystals and macroscopic assembled fibres, Nat. Commun. 2 (2011) 571.
[24] F. Tardani, W. Neri, C. Zakri, H. Kellay, A. Colin, P. Poulin, Shear rheology control of wrinkles and patterns in graphene oxide films, Langmuir 34 (9) (2018) 2996–3002.
[25] Owen C. Compton, Karl W. Putz, Claire Segar, An Zhi, SonBinh T. Nguyen, L. Catherine Brinson, Evolution of order during vacuum assisted self-assembly of graphene oxide paper and associated polymer nanocomposites, ACS Nano 5 (8) (2011) 6601–6609.
[26] K. Li, Z. Han, L. Wang, J. Wang, C. Zhang, J. Lin, S. Luo, L. Peng, W. Fang, Y. Liu, Z. Wu, Y. Tan, C. Gao, Z. Xu, Wrinkling modes of graphene oxide assembled on curved surfaces, Nano Res. 16 (2023) 1801–1809.
[27] P. Poulin, R. Jalili, W. Neri, F. Nallet, T. Divoux, A. Colin, S.H. Aboutalebi, G. Wallace, C. Zakri, Superflexibility of graphene oxide, Proc. Natl. Acad. Sci. USA 113 (40) (2016) 11088–11093.
[28] Y. Wei, B. Wang, J. Wu, R. Yang, M.L. Dunn, Bending rigidity and Gaussian bending stiffness of single-layered graphene, Nano Lett. 13 (1) (2013) 26–30.
[29] Y. Zhang, S. Wang, P. Tang, Z. Zhao, Z. Xu, Z.Z. Yu, H.B. Zhang, Realizing spontaneously regular stacking of pristine graphene oxide by a chemical-structure-engineering strategy for mechanically strong macroscopic films, ACS Nano 16 (6) (2022) 8869–8880.
[30] P. Li, M. Yang, Y. Liu, H. Qin, J. Liu, Z. Xu, Y. Liu, F. Meng, J. Lin, F. Wang, C. Gao, Continuous crystalline graphene papers with gigapascal strength by intercalation modulated plasticization, Nat. Commun. 11 (1) (2020) 2645.
[31] F. Guo, Y. Wang, Y. Jiang, Z. Li, Z. Xu, X. Zhao, T. Guo, W. Jiang, C. Gao, Hydroplastic micromolding of 2D sheets, Adv. Mater. 33 (25) (2021), e2008116.
[32] Z. Li, F. Guo, K. Pang, J. Lin, Q. Gao, Y. Chen, D. Chang, Y. Wang, S. Liu, Y. Han, Y. Liu, Z. Xu, C. Gao, Precise thermoplastic processing of graphene oxide layered solid by polymer intercalation, Nano-Micro Lett. 14 (1) (2021) 12.
[33] E.B. Stukalin, J.F. Douglas, K.F. Freed, Plasticization and antiplasticization of polymer melts diluted by low molar mass species, J. Chem. Phys. 132 (8) (2010), 084504.
[34] S. Vinod, C.S. Tiwary, L.D. Machado, S. Ozden, J. Cho, P. Shaw, R. Vajtai, D. S. Galvao, P.M. Ajayan, Strain rate dependent shear plasticity in graphite oxide, Nano Lett. 16 (2) (2016) 1127–1131.
[35] C. Zhang, Y. Fujii, K. Tanaka, Effect of long range interactions on the glass transition temperature of thin polystyrene films, ACS Macro Lett. 1 (11) (2012) 1317–1320.
[36] A. Oberlin, M. Oberlin, Graphitizability of carbonaceous materials as studied by TEM and X-ray diffraction, J. Microsc. 132 (3) (1983) 353–363.
[37] K.H.L.H. Park, Y.B. Kim, S.B. Ambade, S.H. Noh, W. Eom, J.Y. Hwang, W.J. Lee, J. Huang, T.H. Han, Dynamic assembly of liquid crystalline graphene oxide gel fibers for ion transport, Sci. Adv. 4 (2018), eaau2104.
[38] G. Xin, W. Zhu, Y. Deng, J. Cheng, L.T. Zhang, A.J. Chung, S. De, J. Lian, Microfluidics-enabled orientation and microstructure control of macroscopic graphene fibres, Nat. Nanotechnol. 14 (2) (2019) 168–175.
[39] N. Gupta, V.I. Artyukhov, E.S. Penev, B.I. Yakobson, Carbonization with misfusion: fundamental limits of carbon-fiber strength revisited, Adv. Mater. 28 (46) (2016) 10317–10322.
[40] J. Lin, P. Li, Y. Liu, Z. Wang, Y. Wang, X. Ming, C. Gao, Z. Xu, The origin of the sheet size predicament in graphene macroscopic papers, ACS Nano 15 (3) (2021) 4824–4832.
[41] C.C.Y. Natnael Behabtu, Dmitri E. Tsentalovich, Yeshayahu Talmon, Yachin Cohen, Marcin J. Otto, Matteo Pasquali, Strong, light, multifunctional fibers of carbon nanotubes with ultrahigh conductivity, Science 339 (2013) 182–185.
[42] Y. Bai, R. Zhang, X. Ye, Z. Zhu, H. Xie, B. Shen, D. Cai, B. Liu, C. Zhang, Z. Jia, S. Zhang, X. Li, F. Wei, Carbon nanotube bundles with tensile strength over 80 GPa, Nat. Nanotechnol. 13 (7) (2018) 589–595.
[43] L. Gong, I.A. Kinloch, R.J. Young, I. Riaz, R. Jalil, K.S. Novoselov, Interfacial stress transfer in a graphene monolayer nanocomposite, Adv. Mater. 22 (24) (2010) 2694–2697.

[44] Z. Li, R.J. Young, I.A. Kinloch, Interfacial stress transfer in graphene oxide nanocomposites, ACS Appl. Mater. Interfaces 5 (2) (2013) 456–463.
[45] M. Wu, J. Chen, Y. Wen, H. Chen, Y. Li, C. Li, G. Shi, Chemical approach to ultrastiff, strong, and environmentally stable graphene films, ACS Appl. Mater. Interfaces 10 (6) (2018) 5812–5818.
[46] Z. Liu, Z. Li, Z. Xu, Z. Xia, X. Hu, L. Kou, L. Peng, Y. Wei, C. Gao, Wet-spun continuous graphene films, Chem. Mater. 26 (23) (2014) 6786–6795.
[47] M. Cao, X. Wang, W. Cao, X. Fang, B. Wen, J. Yuan, Thermally driven transport and relaxation switching self-powered electromagnetic energy conversion, Small 14 (29) (2018), 1800987.
[48] B. Wen, M. Cao, M. Lu, W. Cao, H. Shi, J. Liu, X. Wang, H. Jin, X. Fang, W. Wang, J. Yuan, Reduced graphene oxides: light-weight and high-efficiency electromagnetic interference shielding at elevated temperatures, Adv. Mater. 26(21) 3484-3489.
[49] Q. Song, F. Ye, L. Kong, Q. Shen, L. Han, L. Feng, G. Yu, Y. Pan, H. Li, Graphene and MXene nanomaterials: toward high-performance electromagnetic wave absorption in gigahertz band range, Adv. Funct. Mater. 30 (31) (2020), 2000475.
[50] M. Hu, B. Mi, Layer-by-layer assembly of graphene oxide membranes via electrostatic interaction, J. Membr. Sci. 469 (2014) 80–87.
[51] I.D. Nicholas, A. Kotov, Janos H. Fendler, Layer-by-layer self-assembly of polyelectrolyte-semiconductor nanoparticle composite films, J. Phys. Chem. C 99 (1995) 13065–13069.
[52] R.S. Yadav, I. Kuřitka, J. Vilcakova, D. Skoda, P. Urbánek, M. Machovsky, M. Masař, L. Kalina, J. Havlica, Lightweight $NiFe_2O_4$-reduced graphene oxide-elastomer nanocomposite flexible sheet for electromagnetic interference shielding application, Compos. Part B-Eng. 166 (2019) 95–111.
[53] S. Pande, A. Chaudhary, D. Patel, B.P. Singh, R.B. Mathur, Mechanical and electrical properties of multiwall carbon nanotube/polycarbonate composites for electrostatic discharge and electromagnetic interference shielding applications, RSC Adv. 4 (27) (2014).
[54] W. Chen, W. Duan, Y. Liu, Q. Wang, F. Qi, Facile fabrication of multifunctional polymer composites based on three-dimensional interconnected networks of graphene and carbon nanotubes, Ind. Eng. Chem. Res. 58 (47) (2019) 21531–21541.
[55] Z. Yu, T. Dai, S. Yuan, H. Zou, P. Liu, Electromagnetic interference shielding performance of anisotropic polyimide/graphene composite aerogels, ACS Appl. Mater. Interfaces 12 (27) (2020) 30990–31001.
[56] Y. Chen, H.-B. Zhang, M. Wang, X. Qian, A. Dasari, Z.-Z. Yu, Phenolic resin-enhanced three-dimensional graphene aerogels and their epoxy nanocomposites with high mechanical and electromagnetic interference shielding performances, Compos. Sci. Technol. 152 (2017) 254–262.
[57] Y. Huangfu, K. Ruan, H. Qiu, Y. Lu, C. Liang, J. Kong, J. Gu, Fabrication and investigation on the PANI/MWCNT/thermally annealed graphene aerogel/epoxy electromagnetic interference shielding nanocomposites, Compos. Appl. Sci. Manuf. 121 (2019) 265–272.
[58] F. Xu, R. Chen, Z. Lin, Y. Qin, Y. Yuan, Y. Li, X. Zhao, M. Yang, X. Sun, S. Wang, Q. Peng, Y. Li, X. He, Superflexible interconnected graphene network nanocomposites for high-performance electromagnetic interference shielding, ACS Omega 3 (3) (2018) 3599–3607.
[59] X. Yang, S. Fan, Y. Li, Y. Guo, Y. Li, K. Ruan, S. Zhang, J. Zhang, J. Kong, J. Gu, Synchronously improved electromagnetic interference shielding and thermal conductivity for epoxy nanocomposites by constructing 3D copper nanowires/thermally annealed graphene aerogel framework, Compos. Appl. Sci. Manuf. 128 (2020).
[60] Z. Guo, P. Ren, B. Fu, F. Ren, Y. Jin, Z. Sun, Multi-layered graphene-Fe_3O_4/poly (vinylidene fluoride) hybrid composite films for high-efficient electromagnetic shielding, Polym. Test. 89 (2020).
[61] S. Zhang, H. Sun, T. Lan, Z. Bai, X. Liu, Facile preparation of graphene film and sandwiched flexible poly(arylene ether nitrile)/graphene composite films with high EMI shielding efficiency, Compos. Appl. Sci. Manuf. 154 (2022).